

# BRIGHT: Bi-level Feature Representation of Image Collections using Groups of Hash Tables

Dingdong Yang<sup>1</sup> Yizhi Wang<sup>1</sup> Ali Mahdavi-Amiri<sup>1</sup> Hao Zhang<sup>1\*</sup>

<sup>1</sup>School of Computing Science, Simon Fraser University

## Abstract

We present BRIGHT, a *bi-level* feature representation for an image *collection*, consisting of a per-image latent space on top of a multi-scale feature grid space. Our representation is learned by an autoencoder to encode images into *continuous* key codes, which are used to retrieve features from *groups of multi-resolution hash tables*. Our key codes and hash tables are trained together continuously with well-defined gradient flows, leading to high usage of the hash table entries and improved generative modeling compared to discrete Vector Quantization (VQ). Differently from existing continuous representations such as KL-regularized latent codes, our key codes are strictly bounded in scale and variance. Overall, feature encoding by BRIGHT is compact, efficient to train, and enables generative modeling over the image codes using state-of-the-art generators such as latent diffusion models (LDMs). Experimental results show that our method achieves comparable reconstruction results to VQ methods while having a smaller and more efficient decoder network. By applying LDM over our key code space, we achieve state-of-the-art performance on image synthesis on the LSUN-Church and human-face datasets. Project page: <https://bright-project01.github.io/>.

## 1 Introduction

One of the most foundational building blocks of modern-day neural information processing is feature representation learning, whose goal is to map input data into a latent space with desirable properties to uncover useful data patterns and assist the task at hand. Commonly favoured properties of the latent representations include continuity, efficient access, interpretability, compactness while retaining reconstruction quality, as well as generative capabilities reflected by the plausibility and diversity of the generated contents. Classical examples of representation learning include dictionary learning, manifold learning, autoencoders along with other generative models [2, 6].

One notable recent advance in image feature encoding that combines compactness, rapid training, and quality reconstruction is instant neural graphics primitive (instant-NGP) [26]. The key idea was to store feature vectors for a given image in volumetric grids at different scales using *multi-resolution hash tables*. Then, the encoding at a spatial point  $p$  only requires a linear interpolation between the feature vectors at the closest grid nodes that surround  $p$ . Such an encoding can be instantaneously *retrieved* from the hash tables, without running costly neural network predictions. When trained with sufficient samples, instant NGP is able to achieve accurate prediction of a variety of graphics primitives highly efficiently, but it was designed to encode a *single* image.

In this paper, we aim to develop a feature representation for an image *collection* which retains all the advantages of instant NGP, while enabling *generative* modeling over the image codes using state-of-the-art generators such as latent diffusion models (LDMs) [29]; see Figure 1. To this end,

---

\*Corresponding Author.



Figure 1: Image reconstruction results by BRIGHT (row 2) on the validation set of LSUN-church  $256 \times 256$  [39] and FFHQ  $256 \times 256$  datasets [16], where we note the recovery of fine details such as text captions and watermarks. Bottom row shows images generated via latent diffusion trained on key codes from BRIGHT.

our feature representation is necessarily *bi-level*, consisting of a per-image latent space on top of the multi-resolution feature grid space, akin to that of instant NGP. The two spaces should be coherently connected, allow end-to-end training, and suitably support LDMs for image generation, without compromising compactness or efficient access provided by multi-resolution hashing. In addition, the image space must accommodate diversity of the image collection with a sufficiently high dimension, with which we would face a “curse of dimensionality” if only one group of multi-resolution hash tables is employed to encode all the image features, as in instant NGP [26].

To fulfill all the criteria above and address the ensuing challenges, we train a novel autoencoder to represent an image collection, as illustrated in Figures 2 and 3. We encode the image collection using *continuous* key codes at the image level, with one block of keys per image. At the feature level, we use the key codes to retrieve features from, not one, but *groups* of multi-resolution hash tables. With this approach, we retain all the merits of instant NGP while alleviating the “curse of dimensionality.” The retrieved features, after passing through a small MLP, are fed into a StyleGAN-type [17] decoder to reconstruct the input image under the standard autoencoder setting.

Our framework is coined BRIGHT, for Bi-level feature Representation of Image collections using Groups of Hash Tables. Compared to generative models based on discrete Vector Quantization (VQ) [9, 35], which often suffer from low usage rate of their codebooks, our key codes and hash tables are trained together continuously with well-defined gradient flows, leading to high usage of the hash table entries. Differently from existing continuous representations such as KL-regularized latent codes [20], our key codes are strictly bounded in scale and variance. However, the image codes learned by BRIGHT are of high precision and unsuitable for the denoising process in LDMs. We rectify this by injecting a noise perturbation during training to operate on a relaxed data precision.

Experimental results show that BRIGHT achieves comparable reconstruction results to VQ methods while having a much smaller decoder network. By applying LDM over our key code space, we achieve state-of-the-art performance on image synthesis on the LSUN-Church and human-face datasets.

## 2 Related Work

At the core of BRIGHT, we employ hash tables with quantized code entries for image representation and generation. Hence in this section, we focus on discussing the most relevant topics, namely, VQ latent representations, image encoding using hash tables, as well as modern image generators.

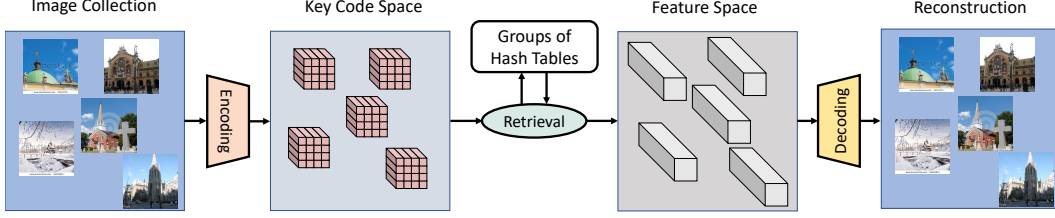


Figure 2: Rather than encoding images into features directly, our method first projects images into key codes and then uses the key codes to retrieve features from groups of hash tables. The encoder, decoder and hash tables are jointly learned under an autoencoder framework.

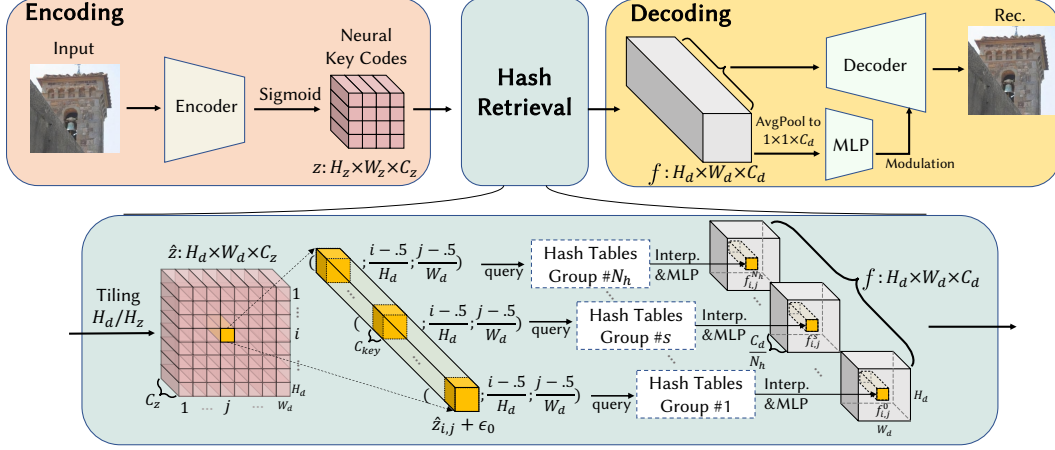


Figure 3: Overall pipeline of our method in three parts: Encoding, Hash Retrieval and Decoding.

## 2.1 Vector Quantized Latent Representation

VQ-VAE [35] proposed to represent the latent codes of data as combinations of discrete codebook entries. VQ-GAN [9] proposed to add a discriminator and perceptual loss to evaluate the reconstructed images, and employed Transformers [36] to model the relationship of codebook entries. RQ-VAE [25] used a residual quantizer to represent an image as a stacked map of discrete codes, resulting in a short sequence of latent codes compared to VQ-GAN. MoVQ [44] proposed to incorporate the spatial information into the quantized vectors so that similar patches within an image do not share the same index. Vanilla VQ methods (VQ-VAE and VQ-GAN) often face the issue of low codebook usage because of ① poor initialization of the codebook, which means only a few codebook entries will be used in the very beginning and ② the training procedure does not guarantee the full coverage of the codebook entries. A codebook entry  $e$  only gets updates from the features that are assigned to it. So dead codes cannot be updated. VIT-VQGAN [40] aims to enhance codebook utilization by reducing its dimensionality and applying  $\mathcal{L}_2$  normalization to the encoded latent vectors.

Our method differs from VQ methods since it performs interpolations on the entries in hash tables. This makes the mapping from key codes to feature vectors continuous. In addition, we utilize a normal stochastic gradient descent algorithm to optimize the entry values in hash tables. Compared to the clustering-based optimization strategy in VQ methods that suffer from usage rate, our method can make full use of the entries (see Section 3.4), thus having a more powerful representation ability.

## 2.2 Image Synthesis via Latent Diffusion

Recently, diffusion models [5, 14, 18, 32] have demonstrated their superiority over VAE [20], GANs [10], Flow-based models [21] in terms of sample quality, ease of training, and scalability. Latent Diffusion Models [29] (LDM) have been proposed to perform diffusion process on the latent codes of images instead of raw pixels. In a vanilla LDM, diffusion is usually performed on the indexings of VQ codebook entries. However, as mentioned above, the VQ codebooks usually suffer

Symbol	Description	Symbol	Description
$z$	key code encoded from input image	$F_r$	spatial hash retrieval function
$\hat{z}$	interleavingly tiled key code	$F_{inp}$	linear interpolation function
$\hat{z}_{i,j}$	tiled key code at spatial location $(i, j)$	$F_{mlp}$	the small MLP network in each group of hash tables
$H_z, W_z$	spatial size of the key code	$N_h$	number of groups of hash tables
$H_d, W_d$	spatial size of the tiled key code	$N_r$	the resolution number of hash tables
$C_z$	channel size of the key code	$C_{key}$	length of a unit key code
$C_d$	channel size of the feature block to decoder	$f_k^v$	feature vectors that encompass $q_{i,j}^s$ in hash tables
$\hat{z}_{i,j}^s$	$s$ -th slice of tiled key code $\hat{z}_{i,j}$	$c_k^v$	coordinates of $f_k^v$
$q_{i,j}^s$	$\hat{z}_{i,j}^s$ combined with spatial coordinates	$f_{i,j}^s$	retrieved feature for every $q_{i,j}^s$

Table 1: Mathematical symbols utilized in our paper along with their descriptions.

from low usage rates. In contrast, the key codes from our representation admit much higher utilization of the hash table entries with improved expressivity. Hence, BRIGHT naturally supports applying LDM on the key codes, leading to image synthesis results with more accurate structures and less distortions.

### 2.3 Image Encoding with Hash Tables

Image hashing is the process of assigning a unique hash value to an image. The hash value is a compact and efficient representation of an image, which facilitates the task of large-scale image retrieval. Deep hashing methods [7, 24, 38, 43] have utilized deep neural networks to map images to compact hash values. However, to the best of our knowledge, hash tables have not been utilized for image generation and reconstruction in the past. Here, we utilize structured and extensive hash tables to represent the feature space of images suitable for image reconstruction and generation. Instead of directly calculating a hash value from image features, our method first outputs spatial-aware keys and then uses them to retrieve values from learnable hash tables shared by all images in a dataset.

Hash tables can also serve as a means to store and compress 3D structural data, resulting in faster accessibility [26, 28, 34]. Instant NGP [26], which provided inspiration for our work, employs multi-resolution hash encoding to accelerate the prediction of graphics primitives such as color, volume density, and signed distance field. SceneDreamer [3] adopts a similar encoding strategy with hash tables to generate large scenes. However, SceneDreamer directly generates scenes with a GAN instead of utilizing the learned key codes as an image representation, as in our work from which a diffusion-based generator is applied. Moreover, rather than using a single series of multi-resolution hash tables, BRIGHT adopts groups of hash tables, where every group of hash tables will be accessed by a slice of our key codes, which is crucial for representing an entire image collection.

## 3 Method

We propose a novel and general method to represent a dataset by compressed continuous key codes and groups of hash tables within an autoencoder framework. The image feature space can be compactly and structurally organized in hash tables. Any image can be encoded by referring to its key code and then performing interpolations on its relevant feature vectors in hash tables.

Our method is comprised of three main components: Encoding, Hash Retrieval, and Decoding (Figure 2). An image is first passed to an encoder to obtain a continuous key code (see Figure 3). Then a hash retrieval is used to retrieve relevant features embeddings stored in hash tables using the key code. An interpolation process is performed on the retrieved features to obtain the feature maps of an input image. Finally, the decoder receives the feature block and reconstructs the image. In the following, we discuss these components in detail and explain their respective functions. We have also provided our mathematical symbols and their descriptions in Table 1.

### 3.1 Encoding

Given an image  $I \in \mathbb{R}^{H \times W \times C}$  with dimension  $H \times W$  and channel width  $C$ , an encoder network is utilized to transform it into a *key code*  $z \in [0, 1]^{H_z \times W_z \times C_z}$  in a *continuous* space, where  $C_z = N_h \times C_{key}$  with  $N_h$  being the number of groups of hash tables and  $C_{key}$  the length of a key unit, each corresponding to one of the hash tables. Our encoder follows the design of VQ-GAN [9], except



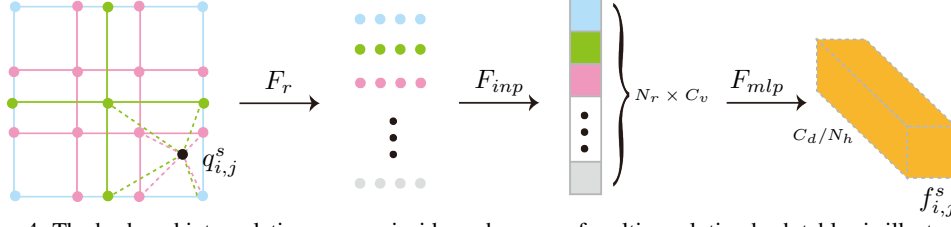


Figure 4: The hash and interpolation process inside each group of multi-resolution hash tables is illustrated for a 2D case. For each combined and sliced key code  $q_{i,j}^s$ , we would retrieve  $F_r$  and interpolate  $F_{inp}$  features across  $N_r$  resolutions. Each resolution will give 4 nodes to be linearly interpolated and each node has dimension  $C_v$ . The feature vectors from all the resolutions will be concatenated as a vector of length  $N_r \times C_v$ . The concatenated feature vector will go through an MLP  $F_{mlp}$  and be projected to be  $f_{i,j}^s$  of length  $C_d/N_h$  as part of the feature block  $f$  to the decoder.

that a sigmoid function is appended to normalize  $z$  into  $[0, 1]$ . This continuous representation  $z$  serves as key to access the multi-resolution hash tables, which provide a grid-based representation of images features over the entire image dataset.

### 3.2 Hash Retrieval

Multi-resolution hash tables [26] consist of tables with varying levels of detail controlled by resolutions. These tables are indexed using a spatial hash function to retrieve entries that are spatially neighboring to encoded keys. The retrieved entries are then linearly interpolated to obtain the image features at the given key. The hash retrieval makes it possible to use continuous key codes to retrieve and interpolate features stored in multi-resolution hash tables for an entire dataset.

Before retrieval from the hash tables, we first tile our continuous code  $z$  interleavily to form a tensor  $\hat{z}$  of size  $H_d \times W_d \times C_z$ , where  $H_d (\geq H_z)$  and  $W_d (\geq W_z)$  are the initial spatial resolution for the decoder (see Figure 3 (Bottom)). The tiling is used to enlarge the spatial size of features that will be sent to decoder. A larger spatial size will result in a smaller and more efficient decoder than previous methods [9, 34, 44]. For each spatial grid  $\hat{z}_{i,j}$  in  $\hat{z}$ , we split its  $C_z$  channels into  $N_h$  slices of codes and each code is in the shape of  $1 \times 1 \times C_{key}$ . It is impossible to construct hash tables that can take  $C_z$ -dimension keys as queries due to computational complexity, so we assign one hash table for each slice of  $C_{key}$ -dimension separately. A small noise  $\epsilon_o \sim \mathcal{N}(0, \frac{1}{(4r_{max})^2})$  is injected in each code slice  $\hat{z}_{i,j}^s$  ( $1 \leq s \leq N_h$ ), where  $r_{max}$  denotes the maximum resolution in a group of multi-resolution hash tables. Perturbed  $\hat{z}_{i,j}^s$  is then concatenated with its normalized spatial coordinates ( $x = \frac{i-0.5}{H_d}, y = \frac{j-0.5}{W_d}$ ) to form a combined key code:

$$q_{i,j}^s = [\hat{z}_{i,j}^s + \epsilon_o; x; y], \quad (1)$$

where  $s$  is the index of slices and  $q_{i,j}^s \in [0, 1]^{C_{key}+2}$ . The minor random perturbation is to construct a relaxed data precision of  $\hat{z}_{i,j}^s$ , which will ease the diffusion training in the second stage (explanations are given in a later section). Incorporating  $(x, y)$  into key codes aims to retrieve spatial-aware features from multi-resolution hash tables. The retrieved features  $f_{i,j}^s$  are then placed into the corresponding location of the feature block  $f \in \mathbb{R}^{H_d \times W_d \times C_d}$ , which serves as the input features to the decoder network (see Figure 3). Mathematically,  $f_{i,j}^s$  is obtained as follows (also see Figure 4):

$$f_{i,j}^s = F_{mlp}(F_{inp}(F_r(q_{i,j}^s))), \quad (2)$$

where,  $F_r$  denotes the hash retrieval function returning the grid nodes that encompass key code  $q_{i,j}^s$  in hash tables. The result of  $F_r$  is a set of tuples  $(f_k^v, c_k^v)$  where  $f_k^v \in \mathbb{R}^{N_r \times C_v}$  contains feature vectors and  $c_k^v \in [0, 1]^{C_{key}+2}$  is their associated coordinates.  $N_r$  is the number of resolutions in each group of hash tables and  $C_v$  is the dimension of feature vectors in hash tables.  $F_r$  is defined as:

$$F_r(q_{i,j}^s) = \{(f_k^v, c_k^v) | 1 \leq k \leq M\}. \quad (3)$$

Here,  $M = 2^{C_{key}+2}$ . For example, if  $C_{key} = 1$ ,  $c_k^v$  will represent the coordinates of a cube and  $f_k^v$  will be the eight feature vectors associated with each of the cube's nodes.

$F_{inp}$  indicates a linear interpolation among  $f_k^v$ s returning a feature vector of size  $N_r \times C_v$  by:

$$\sum_{k=1}^M F_d(c_k^v, q_{i,j}^s) \cdot f_k^v, \quad (4)$$

where  $F_d$  is a distance function from  $c_k^v$ s to  $q_{i,j}^s$ , determining the weight of feature vector  $f_k^v$ . When  $C_{key} = 1$ ,  $F_{inp}$  is a tri-linear interpolation on the cube’s nodes. Finally,  $F_{mlp}$  maps the dimension of interpolated feature vector from  $N_r \times C_v$  into  $C_d/N_h$  using an MLP.

### 3.3 Decoding

The architecture of our decoder follows the design of StyleGAN [17]. The decoder is modulated by a style code  $\in \mathbb{R}^{1 \times 1 \times C_d}$ , which is calculated from  $f$  by average pooling and MLPs.

The entire autoencoding process is trained using ( $\mathcal{L}_2$ ) loss, perceptual loss ( $\mathcal{L}_{percep}$ ) [15], Wasserstein GAN loss ( $\mathcal{L}_{WGAN}$ ) [1] and discriminator’s gradient penalty ( $\mathcal{L}_{gp}$ ) [11]. The total loss is:

$$\mathcal{L}_{total} = \mathcal{L}_2 + \mathcal{L}_{percep} + \mathcal{L}_{WGAN} + \mathcal{L}_{gp}, \quad (5)$$

where the encoder, decoder and hash tables are jointly optimized.

### 3.4 Properties

Here, we discuss four properties of our method that help us improve generation and reconstruction: ① *continuity*, ② *relaxed data precision*, ③ *strictly bounded variance* and it also has a powerful ④ *auxiliary data structure*. We will explain these four properties in the following.

**Continuity.** VQ methods [9, 35] involve using a metric to determine the closest code in a codebook to the encoded feature. The identified code’s gradient is directly applied to the encoded feature during backpropagation. Unlike VQ, our key code and hash tables are trained together continuously with well-defined gradient flows. As illustrated in 2D grids of Figure 5a, the retrieved values at input key code  $(x, y)$  are linearly interpolated by its four encompassing grid nodes and moved in the direction  $\Delta x = [(y_2 - y)(Q_4 - Q_3) + (y - y_1)(Q_2 - Q_1)] \cdot \text{grad}$ , where  $Q_i$  are the value of nodes (a similar derivation can be found for  $y$  direction).

On the other hand, studies [40, 41] have shown that the original VQ method tends to have a very low codebook usage ratio. The non-continuous nature of VQ requires performing careful tricks including a special initialization scheme of the codebook, an alternative distance metric [40] and top-k and top-p (nucleus) sampling heuristics [9]. However, as shown in Figure 5b, all entries in hash tables are hit and the hitting variance is very small in most groups of hash tables. This finding suggests a remarkably even distribution of hits among the entries in our multi-resolution hash tables.

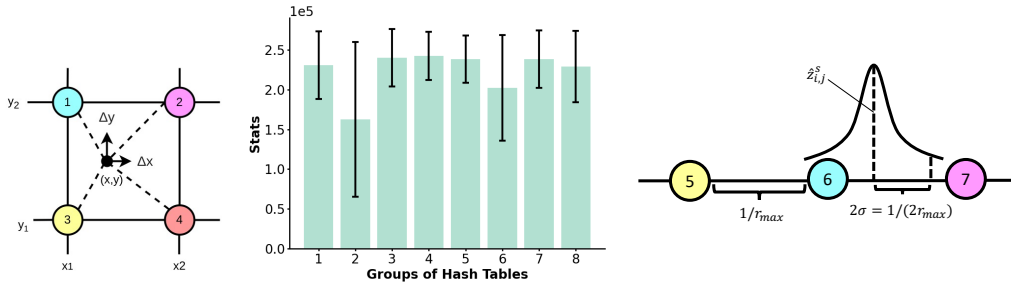


Figure 5(a): The continuous updating mechanism in our method by a linear interpolation of the values of nearby grid nodes.

Figure 5(b): The hitting statistics of hash table entries are shown at the maximum resolution across 8 groups of hash tables ( $N_h = 8, C_z = 8, C_{key} = 1$ ) on the entire training dataset.

Figure 5(c): Relaxed precision mechanism of our method illustrated in 1D grid.  $r_{max}$  is the maximum resolution in multi-resolution hash tables and the colorful circles are grid’s nodes.

**Relaxed Data Precision.** To use our method for image generation, we apply diffusion on key codes. The diffusion process works well on RGB values [5] and generates high-quality data. However, additional considerations are needed when working with latent codes or key codes. For instance,

FFHQ 256×256					LSUN-Church 256×256				
Method	Code Size	LPIPS ↓	SSIM ↑	PSNR ↑	Method	Code Size	LPIPS ↓	SSIM ↑	PSNR ↑
VQGAN [9]	16 × 16	0.1175	0.6641	22.24	VQGAN [9]	32 × 32	0.14±0.07	0.53±0.23	19.81±4.92
RQ-VAE [25]	16 × 16 × 4	0.0895	0.7602	24.53	Ours	32 × 32 × 4	0.12±0.07	0.67±0.20	22.32±5.93
Ours	16 × 16 × 8	0.0885	0.7178	25.72	Ours	32 × 32 × 8	0.07±0.05	0.76±0.17	24.23±6.62
Ours	16 × 16 × 16	<b>0.0522</b>	<b>0.7651</b>	<b>26.99</b>	Ours	64 × 64 × 4	<b>0.04±0.03</b>	<b>0.84±0.13</b>	<b>26.34±7.14</b>

Table 2: Reconstruction metrics on the validation splits of FFHQ [16] and LSUN-Church dataset [39].

Method	VQGAN [9]	VQGAN [9]	RQ-VAE [25]	Ours	Ours	Ours	Ours
Code Size	16×16	32×32	16 × 16 × 4	16 × 16 × 8	16 × 16 × 16	32 × 32 × 4	64 × 64 × 4
Decoder #Parameter	42.5M	13.6M	42.5M	21.2M* + 9.9M	42.9M* + 9.9M	11.4M* + 9.9M	11.4M* + 9.9M
Decoder GFlops	126.79	119.77	126.79	63.54 <sup>‡</sup>	63.80 <sup>‡</sup>	63.40 <sup>‡</sup>	63.40 <sup>‡</sup>

Table 3: Trainable parameters and computational load of decoders. An \* indicates total number of parameters in hash tables and <sup>‡</sup> refers to total computational cost of decoding *and* feature retrieval from hash tables.

LDM [29] proposed to use regularization techniques such as VQ-Reg and KL-Reg to ensure that the latent codes produced by the model are both expressive and tractable. Since we instead work with continuous key codes, we have observed that by relaxing the precision of our key codes, we are able to generate sharper and more accurate data. We do this by injecting a noise  $\epsilon_o \sim \mathcal{N}(0, \frac{1}{(4r_{max})^2})$  to  $\hat{z}_{i,j}^s$  as illustrated in Figure 5c for a simplified 1D grid. After training, the autoencoder learns to produce reasonable reconstruction results from the perturbed key codes as long as they are within the interval of  $\hat{z}_{i,j}^s \pm \frac{1}{2r_{max}}$ . We refer to this design choice as a *relaxed data precision*, with the stipulation that the denoised key codes from BRIGHT do not necessarily need to be high-precision for LDMs to produce high-quality generation results. By setting the std to  $\epsilon_o$  as  $\frac{1}{4r_{max}}$ , the retrieved feature vectors for perturbed  $\hat{z}_{i,j}^s$  will usually vary within three adjacent nodes in hash tables (Figure 5c). The std value strikes a good balance between allowing for greater flexibility in the diffusion process and avoiding excessive uncertainty in the autoencoder. Table 4 shows better reconstructions is obtained when we relax the precision in comparison with non-noisy key codes.

**Strictly Bounded Variance.** For other continuous latent codes [4, 29], KL regularization is utilized to prevent them from growing to codes of arbitrary high variance. However, KL regularization alone cannot ensure a proper upper bound of variance, and excessive weight on KL regularization may harm the reconstruction performance. To address this issue, an element-wise rescaling approach is used on KL-regularized latent codes when training diffusion models, where the rescaling factor is computed from the very first mini-batch of training data [29]. In comparison, our continuous latent codes are keys of hash tables in the range  $[0, 1]$ , and therefore have a strictly bounded variance.

**Auxiliary Data Structure.** Rather than directly passing the encoded features to the decoder for reconstruction, we encode the keys used to retrieve features from an auxiliary data structure, i.e., the multi-resolution hash tables. The multi-resolution hash tables provide powerful feature composition-ability through their multi-resolution hash grids and universal hashing while other continuous latent codes do not have such property [4, 29].

## 4 Results and Evaluation

**Implementation Details and Datasets.** Our experiments are conducted on LSUN-Church [39] and FFHQ [16] datasets. Images in both datasets are resized to  $256 \times 256$ . Our encoder’s architecture is borrowed from the one of VQ-GAN’s [9], while our decoder and discriminator are based on the architecture of StyleGAN2 [17]. We use the unit indexing dimension  $C_{key} = 1$  and the spatial size of  $f$  in the decoder as  $H_d = W_d = 64$ ,  $C_d = 512$  across all the experiments. There are  $N_r = 16$  resolutions in each group of hash tables starting from 4 to 64. Each hash table has maximum  $2^{18}$  entries where each entry contains four float numbers ( $C_v = 4$ ).

When training the autoencoder, we use the Adam optimizer [19] with learning rate  $2e^{-3}$ ,  $\beta_1 = 0$ ,  $\beta_2 = 0.99$  for the encoder, decoder and discriminator. We assign  $\epsilon = 1e^{-8}$  to the Adam optimizer of the discriminator and  $\epsilon = 1e^{-15}$  to the Adam optimizer of the encoder, decoder, and hash tables for quickly updating the hash tables [26].

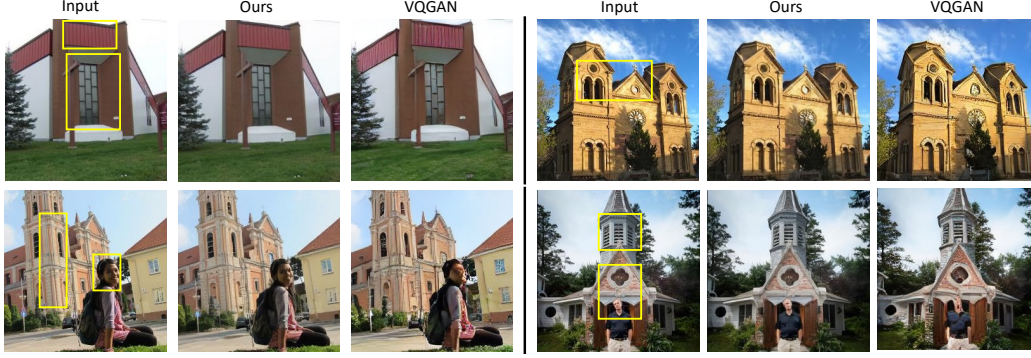


Figure 6: Comparisons to VQGAN [9] demonstrate that our method consistently produces superior reconstruction quality. For optimal viewing and contrast, zoom in on highlighted regions corresponding to the yellow squares.



Figure 7: Image generation by StyleGAN2 [17], LDM [29], and our method on  $256 \times 256$  LSUN-Church dataset [39]. All results shown were selected randomly. Our method clearly outperforms the others in terms of structural coherence and regularity, e.g., less distortion, symmetries (see yellow squares). Red squares highlight significant distortion or structural issues. More results are shown in the supplementary material.

For the diffusion models, we utilize the typical UNet used in networks such as Imagen [30] with unit channel size 256. The UNet is predicting noise [14, 33] with cosine schedule [27] and min-SNR weighting strategy [12]. Training batch size is 128 and the learning rate is  $8e^{-4}$  with linear learning rate warm-up at the first  $1e^4$  training iterations and cosine learning rate decay for  $1e^6$  iterations.

**Comparisons.** For image reconstruction, we compare with SOTA methods including VQ-GAN [9], RQ-VAE [25]. For image synthesis, we compare with Latent Diffusion [29]. Our competitive performance becomes evident when examining the reconstruction metrics (LPIPS [42], SSIM [37], and PSNR) as shown in Table 2. Notably, our approach achieves these commendable results while utilizing a much smaller and more efficient decoder, as shown in Table 3. The qualitative comparison of reconstruction results with VQGAN [9] is shown in Figure 6 indicating that our results have less noise and better preserves details (e.g., the highlighted grid lines in the first image).

For generation, we apply diffusion on the key codes of size  $64 \times 64 \times 4$  on LSUN-Church dataset [39] and FFHQ [16]. Our method is capable of generating high-quality images. The lines of the church building in our results are more straight than those in LDM and our windows are more regularly patterned than StyleGAN2 (Figure 7). Our facial image generation produces superior results compared to LDM [29], with better FID [13] (**8.47 vs 10.77**) and IS [31] (**4.50 vs 4.44**) scores. These evaluations were based on 10.24k samples, some of which are shown in Figure 8. For more quantitative and visual results, please see Appendix C and Appendix D.

**Model Size and Tradeoffs.** The influence of code sizes on both reconstruction quality and model size is shown in Table 2 and Table 3. Our largest model (code size  $16 \times 16 \times 16$ ) has only 10M more parameters ( $\approx 24\%$  increase) than those of the corresponding VQGAN and RQ-VAE models.



Method	Code Size	LPIPS↓	SSIM↑	PSNR↑
Ours (w/o noise)	$32 \times 32 \times 4$	$0.125 \pm 0.072$	$0.6650 \pm 0.208$	$22.29 \pm 6.143$
Ours (with noise)	$32 \times 32 \times 4$	<b><math>0.114 \pm 0.072</math></b>	<b><math>0.6758 \pm 0.199</math></b>	<b><math>22.45 \pm 5.980</math></b>

Table 4: Reconstruction metrics with vs. without noise perturbation on the  $\hat{z}_{i,j}^s$ , evaluated on the validation split of LSUN-Church dataset [39] after training on 800K images.



Figure 8: Randomly selected image generation results, LDM [29] vs. ours, on  $256 \times 256$  FFHQ dataset [16].

However, our model outperforms VQGAN and RQ-VAE across all metrics, showing 55% and 41% improvements in LPIPS, respectively. In terms of computational costs, our method requires  $\approx 50\%$  fewer GFlops due to its smaller decoder and the efficiency gained from utilizing the hash tables.

**Ablation.** To demonstrate the impact of the noise perturbation  $\epsilon_0$ , we compared the reconstruction performance with and without noise (Table 4) showing that the noise perturbation not only does not degrade the reconstruction on the LSUN-Church dataset [39] but leads to slight improvements. These findings provide empirical evidence on the robustness of our method for the reconstruction task. For more parameter studies, please refer to Appendix E.

We also present a comparison of our generated images with the nearest neighbour images obtained from the diffusion training dataset using the LPIPS distance metric [42]. In Figure 9, we show that our generated images are distinct samples rather than mere retrievals from the training dataset.

## 5 Conclusion, Limitation, and Future work

We introduced BRIGHT, a novel bi-level feature representation that leverages a two-step process, where images are initially encoded into continuous key codes organized in blocks. These key codes are employed to retrieve features from groups of multi-resolution hash tables. The key codes in BRIGHT possess desired properties such as continuity, and relaxed data precision that help produce high-quality generation and reconstruction results. Our experimental evaluations showcase that our approach outperforms or achieves comparable reconstruction results to the state-of-the-art Vector Quantization (VQ) methods while employing a smaller and more efficient decoder. Furthermore, the generated results obtained by training a diffusion model on our key codes exhibit high-fidelity and improved structures compared to previous methods. As a limitation, BRIGHT requires more storage compared to existing methods because our hash tables accommodate highly dense feature vectors. It is worthwhile to explore the optimal size of hash tables that strike a balance between compactness and reconstruction/generation quality. It is worth investigating the potential of our method for diverse data types such as videos, scenes, and 3D objects. These data types often exhibit higher redundancy in spatial and temporal dimensions compared to 2D images. The effectiveness of our method, which leverages multi-resolution hash tables and tiled key codes, could prove beneficial for such datasets.

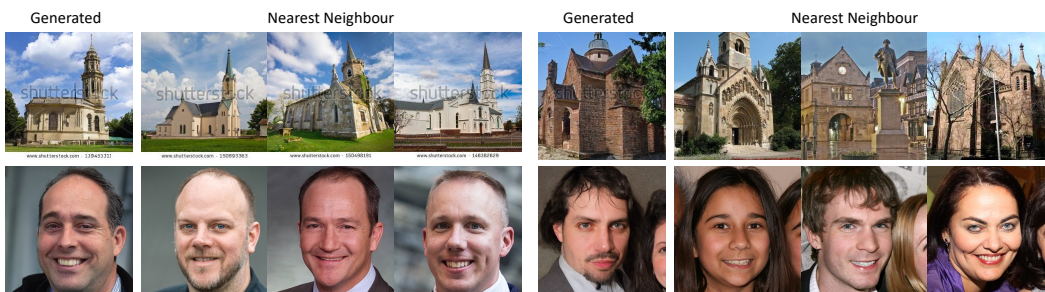


Figure 9: Nearest (by LPIPS [42]) neighbour images of generated samples from the diffusion training dataset.



## References

- [1] Martin Arjovsky, Soumith Chintala, and Léon Bottou. Wasserstein generative adversarial networks. In *International conference on machine learning*, pages 214–223. PMLR, 2017.
- [2] Yoshua Bengio, Aaron Courville, and Pascal Vincent. Representation learning: A review and new perspectives. *IEEE Trans. Pattern Anal. Mach. Intell.*, 35(8):1798–1828, 2012.
- [3] Zhaoxi Chen, Guangcong Wang, and Ziwei Liu. Scenedreamer: Unbounded 3d scene generation from 2d image collections. *arXiv preprint arXiv:2302.01330*, 2023.
- [4] Gene Chou, Yuval Bahat, and Felix Heide. Diffusionsdf: Conditional generative modeling of signed distance functions. *arXiv preprint arXiv:2211.13757*, 2022.
- [5] Prafulla Dhariwal and Alexander Nichol. Diffusion models beat gans on image synthesis. *Advances in Neural Information Processing Systems*, 34:8780–8794, 2021.
- [6] Linus Ericsson, Henry Gouk, Chen Change Loy, and Timothy M. Hospedales. Self-supervised representation learning: Introduction, advances, and challenges. *IEEE Signal Processing*, 2022.
- [7] Venice Erin Liong, Jiwen Lu, Gang Wang, Pierre Moulin, and Jie Zhou. Deep hashing for compact binary codes learning. In *Proceedings of the IEEE conference on computer vision and pattern recognition*, pages 2475–2483, 2015.
- [8] Patrick Esser, Robin Rombach, Andreas Blattmann, and Bjorn Ommer. Imagebart: Bidirectional context with multinomial diffusion for autoregressive image synthesis. *Advances in Neural Information Processing Systems*, 34:3518–3532, 2021.
- [9] Patrick Esser, Robin Rombach, and Bjorn Ommer. Taming transformers for high-resolution image synthesis. In *Proceedings of the IEEE/CVF conference on computer vision and pattern recognition*, pages 12873–12883, 2021.
- [10] Ian Goodfellow, Jean Pouget-Abadie, Mehdi Mirza, Bing Xu, David Warde-Farley, Sherjil Ozair, Aaron Courville, and Yoshua Bengio. Generative adversarial networks. *Communications of the ACM*, 63(11): 139–144, 2020.
- [11] Ishaan Gulrajani, Faruk Ahmed, Martin Arjovsky, Vincent Dumoulin, and Aaron C Courville. Improved training of wasserstein gans. *Advances in neural information processing systems*, 30, 2017.
- [12] Tiankai Hang, Shuyang Gu, Chen Li, Jianmin Bao, Dong Chen, Han Hu, Xin Geng, and Baining Guo. Efficient diffusion training via min-snr weighting strategy. *arXiv preprint arXiv:2303.09556*, 2023.
- [13] Martin Heusel, Hubert Ramsauer, Thomas Unterthiner, Bernhard Nessler, and Sepp Hochreiter. Gans trained by a two time-scale update rule converge to a local nash equilibrium. *Advances in neural information processing systems*, 30, 2017.
- [14] Jonathan Ho, Ajay Jain, and Pieter Abbeel. Denoising diffusion probabilistic models. *Advances in Neural Information Processing Systems*, 33:6840–6851, 2020.
- [15] Justin Johnson, Alexandre Alahi, and Li Fei-Fei. Perceptual losses for real-time style transfer and super-resolution. In *Computer Vision—ECCV 2016: 14th European Conference, Amsterdam, The Netherlands, October 11–14, 2016, Proceedings, Part II 14*, pages 694–711. Springer, 2016.
- [16] Tero Karras, Samuli Laine, and Timo Aila. A style-based generator architecture for generative adversarial networks. In *Proceedings of the IEEE/CVF conference on computer vision and pattern recognition*, pages 4401–4410, 2019.
- [17] Tero Karras, Samuli Laine, Miika Aittala, Janne Hellsten, Jaakko Lehtinen, and Timo Aila. Analyzing and improving the image quality of stylegan. In *Proceedings of the IEEE/CVF conference on computer vision and pattern recognition*, pages 8110–8119, 2020.
- [18] Diederik Kingma, Tim Salimans, Ben Poole, and Jonathan Ho. Variational diffusion models. *Advances in neural information processing systems*, 34:21696–21707, 2021.
- [19] Diederik P Kingma and Jimmy Ba. Adam: A method for stochastic optimization. *arXiv preprint arXiv:1412.6980*, 2014.
- [20] Diederik P Kingma and Max Welling. Auto-encoding variational bayes. *arXiv preprint arXiv:1312.6114*, 2013.
- [21] Durk P Kingma and Prafulla Dhariwal. Glow: Generative flow with invertible 1x1 convolutions. *Advances in neural information processing systems*, 31, 2018.
- [22] Tuomas Kynkäänniemi, Tero Karras, Samuli Laine, Jaakko Lehtinen, and Timo Aila. Improved precision and recall metric for assessing generative models. *Advances in Neural Information Processing Systems*, 32, 2019.
- [23] Tuomas Kynkäänniemi, Tero Karras, Miika Aittala, Timo Aila, and Jaakko Lehtinen. The role of imagenet classes in fr<sup>2</sup> inception distance. *arXiv preprint arXiv:2203.06026*, 2022.

- [24] Hanjiang Lai, Yan Pan, Ye Liu, and Shuicheng Yan. Simultaneous feature learning and hash coding with deep neural networks. In *Proceedings of the IEEE conference on computer vision and pattern recognition*, pages 3270–3278, 2015.
- [25] Doyup Lee, Chihyeon Kim, Saehoon Kim, Minsu Cho, and Wook-Shin Han. Autoregressive image generation using residual quantization. In *Proceedings of the IEEE/CVF Conference on Computer Vision and Pattern Recognition*, pages 11523–11532, 2022.
- [26] Thomas Müller, Alex Evans, Christoph Schied, and Alexander Keller. Instant neural graphics primitives with a multiresolution hash encoding. *ACM Transactions on Graphics (ToG)*, 41(4):1–15, 2022.
- [27] Alexander Quinn Nichol and Prafulla Dhariwal. Improved denoising diffusion probabilistic models. In *International Conference on Machine Learning*, pages 8162–8171. PMLR, 2021.
- [28] Matthias Nießner, Michael Zollhöfer, Shahram Izadi, and Marc Stamminger. Real-time 3d reconstruction at scale using voxel hashing. *ACM Transactions on Graphics (ToG)*, 32(6):1–11, 2013.
- [29] Robin Rombach, Andreas Blattmann, Dominik Lorenz, Patrick Esser, and Björn Ommer. High-resolution image synthesis with latent diffusion models. In *Proceedings of the IEEE/CVF Conference on Computer Vision and Pattern Recognition*, pages 10684–10695, 2022.
- [30] Chitwan Saharia, William Chan, Saurabh Saxena, Lala Li, Jay Whang, Emily L Denton, Kamyar Ghasemipour, Raphael Gontijo Lopes, Burcu Karagol Ayan, Tim Salimans, et al. Photorealistic text-to-image diffusion models with deep language understanding. *Advances in Neural Information Processing Systems*, 35:36479–36494, 2022.
- [31] Tim Salimans, Ian Goodfellow, Wojciech Zaremba, Vicki Cheung, Alec Radford, and Xi Chen. Improved techniques for training gans. *Advances in neural information processing systems*, 29, 2016.
- [32] Jascha Sohl-Dickstein, Eric Weiss, Niru Maheswaranathan, and Surya Ganguli. Deep unsupervised learning using nonequilibrium thermodynamics. In *International Conference on Machine Learning*, pages 2256–2265. PMLR, 2015.
- [33] Yang Song, Jascha Sohl-Dickstein, Diederik P Kingma, Abhishek Kumar, Stefano Ermon, and Ben Poole. Score-based generative modeling through stochastic differential equations. *arXiv preprint arXiv:2011.13456*, 2020.
- [34] Matthias Teschner, Bruno Heidelberger, Matthias Müller, Danat Pomerantes, and Markus H Gross. Optimized spatial hashing for collision detection of deformable objects. In *Vmv*, volume 3, pages 47–54, 2003.
- [35] Aaron Van Den Oord, Oriol Vinyals, et al. Neural discrete representation learning. *Advances in neural information processing systems*, 30, 2017.
- [36] Ashish Vaswani, Noam Shazeer, Niki Parmar, Jakob Uszkoreit, Llion Jones, Aidan N Gomez, Łukasz Kaiser, and Illia Polosukhin. Attention is all you need. *Advances in neural information processing systems*, 30, 2017.
- [37] Zhou Wang, Alan C Bovik, Hamid R Sheikh, and Eero P Simoncelli. Image quality assessment: from error visibility to structural similarity. *IEEE transactions on image processing*, 13(4):600–612, 2004.
- [38] Rongkai Xia, Yan Pan, Hanjiang Lai, Cong Liu, and Shuicheng Yan. Supervised hashing for image retrieval via image representation learning. In *Proceedings of the AAAI conference on artificial intelligence*, volume 28, 2014.
- [39] Fisher Yu, Ari Seff, Yinda Zhang, Shuran Song, Thomas Funkhouser, and Jianxiong Xiao. Lsun: Construction of a large-scale image dataset using deep learning with humans in the loop. *arXiv preprint arXiv:1506.03365*, 2015.
- [40] Jiahui Yu, Xin Li, Jing Yu Koh, Han Zhang, Ruoming Pang, James Qin, Alexander Ku, Yuanzhong Xu, Jason Baldridge, and Yonghui Wu. Vector-quantized image modeling with improved vqgan. *arXiv preprint arXiv:2110.04627*, 2021.
- [41] Neil Zeghidour, Alejandro Luebs, Ahmed Omran, Jan Skoglund, and Marco Tagliasacchi. Soundstream: An end-to-end neural audio codec, 2021.
- [42] Richard Zhang, Phillip Isola, Alexei A Efros, Eli Shechtman, and Oliver Wang. The unreasonable effectiveness of deep features as a perceptual metric. In *Proceedings of the IEEE conference on computer vision and pattern recognition*, pages 586–595, 2018.
- [43] Fang Zhao, Yongzhen Huang, Liang Wang, and Tieniu Tan. Deep semantic ranking based hashing for multi-label image retrieval. In *Proceedings of the IEEE conference on computer vision and pattern recognition*, pages 1556–1564, 2015.
- [44] Chuanxia Zheng, Tung-Long Vuong, Jianfei Cai, and Dinh Phung. Movq: Modulating quantized vectors for high-fidelity image generation. *Advances in Neural Information Processing Systems*, 35:23412–23425, 2022.

## A More Implementation Details

### A.1 Detailed Architecture of the Encoder

For more details about the Encoder, please refer to the official implementation<sup>2</sup> of VQGAN [9]. We use the same implementation but set the attention resolution from 64 to  $\min(H_z, W_z)$  and the unit channel size as 32.

### A.2 Detailed Architecture of the UNet for Denoising

Following the design of LDM [29], we use a UNet with channel multiplier of (1, 2, 3, 4), 2 residual blocks in each resolution and attention at resolutions 32, 16, 8.

### A.3 Loss Weights of Training Autoencoder

We set the weight of  $L_2$  loss as 20 and the weight of  $L_{percep}$  as 5. The weight on gradient penalty is 4 across all experiments.

## B Evaluation Metrics

To evaluate the **reconstruction** results, we adopt metrics including LPIPS [42], SSIM [37] and PSNR. To evaluate the **generated** results, we adopt metrics including FID [13], CLIP-FID [23], Inception Score (IS) [31], and Precision-Recall [22]. According to a recent study [23], FID is known to sometimes disagree with human judgment. FID may be improved substantially without actually improving the generation quality because of some intentional or accidental distortions that are aligned with the feature space of the classes in the dataset. Therefore, we also use CLIP-FID as an additional metric to FID. The F1 score ( $F_1$ ) is a harmonic mean of precision ( $P$ ) and recall ( $R$ ):

$$F_1 = \frac{2 \cdot P \cdot R}{P + R}. \quad (6)$$

Our evaluation scripts are built on widely-used Python libraries: *torchmetrics*<sup>3</sup>, *torch-fidelity*<sup>4</sup>, *clean-fid*<sup>5</sup> and a 3rd-party repo<sup>6</sup>. All the evaluation scripts will be included in our code to be released.

## C More Results on FFHQ [16] Dataset

We report quantitative results in Table 5 evaluated from 50K sampled images. Our method achieves the best scores of CLIP-FID, IS and precision among all compared methods. The precision of our generated images is significantly higher than others, indicating a substantial reduction of low-quality samples in our results. While our recall is almost the same as StyleGAN, it is lower than LDM. For LDM, we have noticed a disparity between the FID calculated using the checkpoint released by the authors and the value reported in the paper [29], which was also discussed in *a github issue*<sup>7</sup>.

We showcase more visual results in Figure 10 from FFHQ. From the uncurated samples, we can see that the diffusion model trained on our key codes is able to generate high-fidelity human faces with diverse races, ages, hair styles, poses, accessories and so on. Moreover, we also provide more nearest neighbour results in Figure 11 to restate that even with much higher precision score, our generated results are unique samples and not mere retrievals from the training set.

---

<sup>2</sup><https://github.com/CompVis/taming-transformers/blob/master/taming/modules/diffusionmodules/model.py>

<sup>3</sup><https://torchmetrics.readthedocs.io/en/stable/>

<sup>4</sup><https://github.com/toshas/torch-fidelity>

<sup>5</sup><https://github.com/GaParmar/clean-fid>

<sup>6</sup><https://github.com/youngjung/improved-precision-and-recall-metric-pytorch>

<sup>7</sup><https://github.com/CompVis/latent-diffusion/issues/138>

Method	FID ↓	CLIP-FID ↓	IS ↑	Precision ↑	Recall ↑	F1-score ↑
ImageBART [8]	10.81	-	4.49	-	-	-
StyleGAN2 [17]	<b>4.16</b>	2.76 <sup>†</sup>	-	0.71	0.46	0.558
LDM [29]	4.98	-	4.50	0.73	0.50	<b>0.593</b>
LDM* [29]	9.47	3.21	4.47	0.64	<b>0.54</b>	0.585
Ours	6.91	<b>2.66</b>	<b>4.56</b>	<b>0.80</b>	0.45	0.574

Table 5: Quantitative results of generation on FFHQ dataset [16]. All methods are evaluated on 50K sampled images. \* denotes the results calculated using the checkpoint released by LDM authors on Github. The CLIP-FID (<sup>†</sup>) of StyleGAN2 is reported by another work [23].

## D More Results on LSUN-Church [39] Dataset

We report quantitative results of generation on LSUN-Church in Table 6 from 50K sampled images. Our method produces competitive FID and Inception Scores compared to LDM [29] and StyleGAN2 [17]. Similar to the finding in FFHQ, our method gets  $\sim 20\%$  higher precision score than LDM and StyleGAN2.

We showcase more visual results Figure 12 from LSUN-Church. As we can see from the uncurated samples, our method *consistently* generates diverse church buildings with good overall structures and details, coinciding with our high precision score. We also provide more nearest neighbour results in Figure 13. In addition, we show more uncurated samples from LDM [29] in Figure 14 to highlight their difference with our results. Generated images from LDM sometimes lack symmetry, and also have bent columns and unstructured windows. We use **red** squares to highlight such distortions of LDM results in Figure 14 and **yellow** squares to highlight our structured and symmetric results in Figure 12.

Method	FID ↓	CLIP-FID ↓	IS ↑	Precision ↑	Recall ↑	F1-score ↑
DDPM [14]	7.89	-	-	-	-	-
StyleGAN2 [17]	<b>3.86</b>	<b>7.46</b>	<b>2.76</b>	0.63	0.43	0.511
LDM [29]	4.02	-	2.72	0.64	<b>0.52</b>	<b>0.573</b>
Ours	4.66	8.52	2.56	<b>0.78</b>	0.41	0.537

Table 6: Quantitative results of generation on LSUN-Church dataset [39]. All methods are evaluated on 50K sampled images.

## E Parameter Studies

### E.1 The Setting of $C_{key}$

In this section, we discuss how the value of  $C_{key}$ , i.e., the length of a key unit, will affect the performance and complexity of our method. We tested  $C_{key} \in \{1, 2\}$  with the code size of  $64 \times 64 \times 4$ , and kept all other hyper-parameters fixed. As shown in Table 7, increasing  $C_{key}$  from 1 to 2 leads to a marginal improvement in reconstruction metrics on the LSUN-Church [39] validation split. However, it brings a significant increase of the size of hash tables, from 11.4M to 30.5M. The increase is due to the fact that, for each resolution  $r$  of the hash tables, the total number of parameters is  $\min(r^{2+C_{key}}, 2^{18})$ , where  $2^{18}$  is the maximum allowed entry number for each hash table. Therefore, there exists a trade-off between performance and the amount of hash table parameters. We choose  $C_{key} = 1$  as the default setting in our paper.

### E.2 The Setting of $H_d$ and $W_d$

We also investigated the impact of adjusting the values of  $(H_d, W_d)$ , i.e., the resolution of feature blocks that are sent to the decoder. We tested  $(H_d, W_d) \in \{(64, 64), (32, 32)\}$  with the code size of  $32 \times 32 \times 8$ . When  $(H_d, W_d) = (64, 64)$ , the key code will be tiled from  $32 \times 32 \times 8$  to  $64 \times 64 \times 8$ .

Method	Code size	$C_{key}$	LPIPS↓	SSIM↑	PSNR↑	Decoder #Parameter	Decoder GFlops
Ours	$64 \times 64 \times 4$	1	$0.0383 \pm 0.0312$	$0.8438 \pm 0.1295$	$26.34 \pm 7.136$	<b>11.4M* + 9.9M</b>	<b>63.40</b>
Ours	$64 \times 64 \times 4$	2	<b>0.0365 ± 0.0297</b>	<b>0.8480 ± 0.1282</b>	<b>26.47 ± 7.289</b>	30.5M* + 9.9M	<b>63.40</b>

Table 7: Ablation study on  $C_{key}$  on LSUN-Church [39]. \* indicates the total number of parameters in hash tables.

When  $(H_d, W_d) = (32, 32)$ , an additional convolution block is required to bring up the resolution from 32 to 64 in the decoder, yielding more training parameters and computation. As shown in Table 8, setting  $(H_d, W_d) = (64, 64)$  both reduces the computational complexity and offers slightly better reconstruction performance. Therefore, we choose  $(H_d, W_d) = (64, 64)$  as the default setting in our paper.

Method	Code size	$H_d, W_d$	LPIPS↓	SSIM↑	PSNR↑	Decoder #Parameter	Decoder GFlops
Ours	$32 \times 32 \times 8$	64, 64	<b>0.0697 ± 0.0516</b>	<b>0.7576 ± 0.1735</b>	<b>24.23 ± 6.622</b>	<b>21.2M* + 9.9M</b>	<b>63.54</b>
Ours	$32 \times 32 \times 8$	32, 32	$0.0690 \pm 0.0505$	$0.7466 \pm 0.1799$	$24.06 \pm 6.713$	3.7M* + 35.1M	85.14

Table 8: Ablation study on  $H_d, W_d$  on LSUN-Church [39]. An \* indicates total total number of parameters in hash tables.





Figure 10: Uncurated samples of our generation results on FFHQ  $256 \times 256$ .





Figure 11: Nearest (by LPIPS [42]) neighbours of uncured samples of our generation results on FFHQ  $256 \times 256$ . The **leftmost** images in each row are the generated samples and the rest images in each row are nearest neighbours in training dataset.





Figure 12: Uncurated samples of our generated results on LSUN-Church  $256 \times 256$ . Yellow squares highlight some of our structured and symmetric results.





Figure 13: Nearest (by LPIPS [42]) neighbours of uncurated samples of our generation results on LSUN-Church  $256 \times 256$ . The **leftmost** images in each row are the generated samples and the rest images in each row are nearest neighbours in training dataset.





Figure 14: Uncurated samples of LDM [29] generation results on LSUN-Church  $256 \times 256$ . Red squares highlight some structural issues in LDM results.